Author for correspondence:
H. Droogendijk
e-mail: h.droogendijk@utwente.nl

Towards a biomimetic gyroscope inspired by the fly's haltere using microelectromechanical systems technology

H. Droogendijk, R. A. Brookhuis, M. J. de Boer, R. G. P. Sanders and G. J. M. Krijnen

MESA+ Institute for Nanotechnology, University of Twente, Enschede, The Netherlands

Flies use so-called halteres to sense body rotation based on Coriolis forces for supporting equilibrium reflexes. Inspired by these halteres, a biomimetic gimbal-suspended gyroscope has been developed using microelectromechanical systems (MEMS) technology. Design rules for this type of gyroscope are derived, in which the haltere-inspired MEMS gyroscope is geared towards a large measurement bandwidth and a fast response, rather than towards a high responsivity. Measurements for the biomimetic gyroscope indicate a (drive mode) resonance frequency of about 550 Hz and a damping ratio of 0.9. Further, the theoretical performance of the fly's gyroscopic system and the developed MEMS haltere-based gyroscope is assessed and the potential of this MEMS gyroscope is discussed.

1. Introduction

In biology, insects regularly use mechanosensory mechanisms for measurement of physical quantities such as acceleration, flow and rotational rate [1]. For example, a cricket uses club-shaped (clavate) hairs to compensate head movement when it is rotated around its longitudinal axis [2]. In addition, bristle hairs are found on the cricket, which are shown to be sensitive to tactile stimuli. Furthermore, filiform hairs are present at the cricket's cerci for measurement of low-frequency airflows [3,4].

Another example of a biological sensory system that exploits a cylinder-like mechanical structure are the fly's halteres. Halteres are tiny club-shaped organs that beat in anti-phase to the wings during flight [5], and function as gyroscopes[1] by measuring the flies body rotation using Coriolis forces [6]. The rotation-dependent position of the haltere (figure 1) is measured in fields of sensitive strain receptors, campaniform sensilla [7]. It has been demonstrated that this haltere-based system is used for supporting equilibrium reflexes [8–11].

For measuring angular rate, numerous types of gyroscopes have been realized over the past years using MEMS technology, where current state-of-the-art MEMS gyroscopes show formidable performance in range, resolution and noise floor [12–15]. MEMS gyroscopes are typically no haltere-based systems, are generally heavily underdamped[2] and operate at rather high frequencies. By contrast, the fly's haltere system is a close to critically damped system and operates around the fly's wing beat frequency (130–150 Hz) [9]. Obviously, the fly's haltere system has developed under evolutionary pressure and therefore addresses the sensory needs of the fly. As a result, not only the operation principle is different from those generally used in MEMS gyroscopes, but also the performance may score high on metrics other than generally used for MEMS gyroscopes. For example, bandwidth and response time may be far more essential for flies than (bias-)stability and noise floor, as the halteres have been proven to aid in flight dynamics of flies with fast (less than 10 ms) responses to flight disturbances [16].
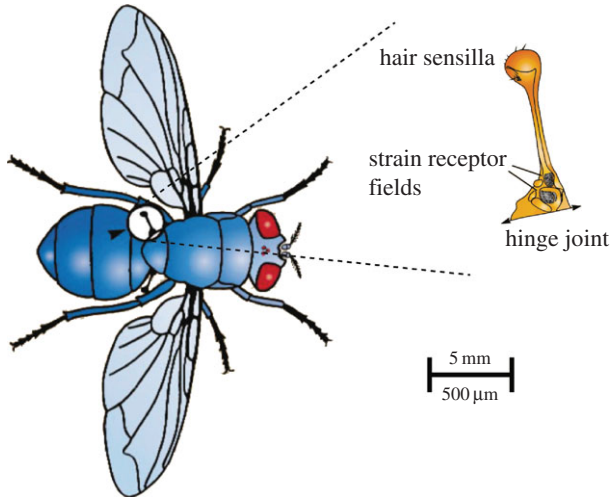
Figure 1. Halteres of the blowfly *Calliphora vicina*. During walking and flight, the halteres oscillate in a vertical plane around a proximal hinge (adapted from [7]). (Online version in colour.)

Previous research on bioinspired gyroscopic systems (using foils of stainless steel) shows advantages on using a haltere-based gyroscope by achieving a higher sensitivity and a lower power consumption compared with conventional MEMS gyroscopes [17,18]. In addition, Tang *et al.* [19] and Challoner *et al.* [20] fabricated haltere-based gyroscopes using MEMS technology, although these devices had still macroscopic dimensions compared with the fly's haltere and were severely underdamped by operating them in vacuum. Wicaksono *et al.* [21] discuss the preliminary design and modelling of a bioinspired MEMS gyroscope with electrostatic driving and piezo-resistive read-out. Smith *et al.* [22] report on the design and fabrication of an MEMS haltere-like structure to use as a sensor in a micro-autonomous system.

In our work, we aim for the design, fabrication and optimization of a biomimetic gyroscope using MEMS technology and haltere-like dimensions. By doing so, we intend to investigate some of the intricacies of the working principle of the haltere system and assess its usability with respect to engineering applications by considering dimensions comparable to the fly's haltere.

2. Theory and modelling

2.1. Mechanics

The dynamics of the haltere-based gyroscope and common MEMS gyroscopes are similar, because both types consist of vibrating structures governed by two coupled second-order differential equations. The design of these gyroscopes is, in general, a two-dimensional isotropic, damped mass-spring system. To describe the haltere mechanics, we first define the force F acting on the haltere knob [23]:

$$F = mg - m\ddot{r}_i - ma_f - m\dot{\Omega} \times r_i - m\Omega \times (\Omega \times r_i) - 2m\Omega \times \dot{r}_i, \tag{2.1}$$

where $\times$ denotes the vector product, m is the mass of the knob, g is the gravitational acceleration, r_i is the position of the knob with respect to the fly, a_f is the linear acceleration of the fly in space and Ω is the angular rate. Six forces contribute to the total inertial force: gravitational (mg), primary ($m\ddot{r}$), linear
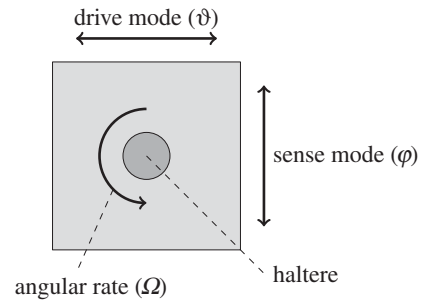
acceleration (ma_f), angular acceleration ($m\dot{\Omega} \times r_i$), centrifugal ($m\Omega \times (\Omega \times r_i)$) and Coriolis ($-2m\Omega \times \dot{r}_i$).

Now, we assume that linear accelerations are absent ($a_f = 0$), gravitational acceleration g is present only in the z-direction (the axial direction of the haltere), angular rates are applied only in the horizontal xy-plane ($\Omega_x = \Omega_y = 0$), the movement of the haltere is harmonic with frequency ω and the angular rate Ω is harmonic with frequency ν and amplitude Ω_0

$$\Omega = \Omega_0 \cos(\nu t) = \frac{1}{2}\Omega_0(e^{j\nu t} + e^{-j\nu t}). \tag{2.2}$$

Consequently, the force amplitude F for the x- and y-direction, because the z-direction is not of interest to us, is given by

$$F_0 = m \begin{bmatrix} \omega^2 + \frac{1}{2}\Omega_0^2 + \frac{1}{2}\Omega_0^2\cos(2\nu t) & -j2\omega\Omega_0\cos(\nu t) + j\nu\Omega_0\sin(\nu t) \\ j2\omega\Omega_0\cos(\nu t) - j\nu\Omega_0\sin(\nu t) & \omega^2 + \frac{1}{2}\Omega_0^2 + \frac{1}{2}\Omega_0^2\cos(2\nu t) \end{bmatrix} \\ \times \begin{bmatrix} x_0 \\ y_0 \end{bmatrix}, \tag{2.3}$$

where x_0 and y_0 denote the amplitudes in the x- and y-direction, respectively. Now, the coordinate system is changed into cylindrical coordinates, as shown in figure 2. The system is continuously driven in a steady-state rotational motion in the drive mode with angle ϑ. Any non-zero rotation-rate reorientation of the halteres' beating plane will induce Coriolis forces impeding on the sense mode, with the corresponding angle φ proportional to the input angular rate Ω. By using the following relationships, the force acting on the haltere can be written as a torque T for small angle amplitudes ϑ_0 and φ_0:

$$J = \eta mL^2, \quad x_0 = L\sin(\vartheta_0) \approx L\vartheta_0, \quad y_0 = L\sin(\varphi_0) \approx L\varphi_0, \tag{2.4}$$

where L is the haltere length, J is the moment of inertia and η is a parameter depending on the precise geometry. Here, $\eta = 1$ by considering the haltere knob as a point mass. As a result, the torque acting on the haltere becomes

$$\vec{T} = J \begin{bmatrix} \omega^2 + \frac{1}{2}\Omega_0^2 + \frac{1}{2}\Omega_0^2\cos(2\nu t) & -j2\omega\Omega_0\cos(\nu t) + j\nu\Omega_0\sin(\nu t) \\ j2\omega\Omega_0\cos(\nu t) - j\nu\Omega_0\sin(\nu t) & \omega^2 + \frac{1}{2}\Omega_0^2 + \frac{1}{2}\Omega_0^2\cos(2\nu t) \end{bmatrix} \\ \times \begin{bmatrix} \vartheta_0 \\ \varphi_0 \end{bmatrix}. \tag{2.5}$$

The torque T acts on the haltere, which is part of the isotropic gyroscopic mechanical system. The response of this system is

Figure 2. Operation principle of the biomimetic gyroscope (top view).

described by a coupled second-order differential equation

$$
\begin{bmatrix} G(\omega, v) & -C(\omega, v) \\ C(\omega, v) & G(\omega, v) \end{bmatrix} \begin{bmatrix} \vartheta_0 \\ \varphi_0 \end{bmatrix} = \begin{bmatrix} \mathcal{T}_{\text{ext}} \\ 0 \end{bmatrix}, \tag{2.6}
$$

where $G(\omega, v)$ is given by

$$
G(\omega, v) = -\omega^2 + j2\zeta\omega\omega_0 + \omega_0^2 - \frac{1}{2}\Omega_0^2[1 + \cos(2vt)], \tag{2.7}
$$

and $C(\omega, v)$ denotes the coupling between the drive and sense mode owing to angular rates

$$
C(\omega, v) = j2\omega\Omega_0\cos(vt) - jv\Omega_0\sin(vt). \tag{2.8}
$$

In these expressions, the resonance frequency ω_0, damping ratio ζ and normalized driving torque $\mathcal{T}_{\text{ext}}$ are defined as

$$
\omega_0 = \sqrt{\frac{S}{J}}, \quad \zeta = \frac{R}{2\sqrt{SJ}} \quad \text{and} \quad \mathcal{T}_{\text{ext}} = \frac{T_0}{J}. \tag{2.9}
$$

where T_0 is the driving torque,[3] S is the torsional stiffness, R is the torsional resistance and J is the moment of inertia. Further, ϑ_0 and φ_0 are the amplitudes of respectively drive and sense mode. For constant angular rates ($v = 0$), the second-order mechanical system reduces to

$$
\begin{bmatrix} -\omega^2 + j2\zeta\omega\omega_0 + \omega_0^2 - \Omega_0^2 & -j2\omega\Omega_0 \\ j2\omega\Omega_0 & -\omega^2 + j2\zeta\omega\omega_0 + \omega_0^2 - \Omega_0^2 \end{bmatrix}
$$
$$
\times \begin{bmatrix} \vartheta_0 \\ \varphi_0 \end{bmatrix} = \begin{bmatrix} \mathcal{T}_{\text{ext}} \\ 0 \end{bmatrix}. \tag{2.10}
$$

It follows from (2.6) and (2.10) that the exposure to an angular rate Ω clearly affects the system's behaviour; its resonance frequency is reduced by centrifugal forces, and torque contributions by angular Coriolis forces cause coupling between drive and sense mode. Although the reduction in resonance frequency by Ω_0^2 is typically negligible, the principle of a rate-dependent resonance frequency can be used for gyroscopic measurement of large angular rates [24].

2.2. Design rules

The governing equation of motion for the drive mode including its amplitude has already been stated in (2.6). By driving the gyroscope by a harmonic torque, assuming that the angular rate Ω is small compared with the sensor's resonance frequency ($\Omega_0 \ll \omega_0$), and angular accelerations are small ($v \ll \omega$), the drive-mode amplitude ϑ_0 can be approximated well by

$$
\vartheta_0(\omega) = \frac{\mathcal{T}_{\text{ext}}}{\sqrt{(\omega_0^2 - \omega^2)^2 + (2\zeta\omega_0\omega)^2}}. \tag{2.11}
$$

Generally, MEMS gyroscopes are driven at a frequency ω equal to the gyroscope's resonance frequency ω_0 in the case of underdamped systems. Then, the drive-mode amplitude can be simplified to

$$
\vartheta_0 = \frac{\mathcal{T}_{\text{ext}}}{2\zeta\omega_0^2}. \tag{2.12}
$$

Based on the drive-mode motion, the normalized Coriolis-induced torque $\mathcal{T}_c$ amplitude of the sense mode is given by

$$
\mathcal{T}_c = 2\omega_0\vartheta_0\Omega_0. \tag{2.13}
$$

Using the system of equations of (2.6), the corresponding sense mode amplitude φ_0 can be approximated as

$$
\varphi_0 = \frac{\mathcal{T}_{\text{ext}}}{2}\frac{1}{\omega_0^3\zeta^2}\Omega_0. \tag{2.14}
$$

Now, we define the ratio $\mathcal{R}$ between sense and drive-mode amplitudes, which is a measure for the system's responsivity.[4] Because Coriolis forces in general are small, a large $\mathcal{R}$ is desirable in order to measure correspondingly small angular rates Ω. The ratio $\mathcal{R}$ is defined as

$$
\mathcal{R} = \frac{\mathrm{d}}{\mathrm{d}\Omega_0}\left(\frac{\varphi_0}{\vartheta_0}\right) = \kappa. \tag{2.15}
$$

where κ is a design parameter, which is the reciprocal of the product of damping ratio ζ and resonance frequency ω_0

$$
\kappa = \frac{1}{\zeta\omega_0}. \tag{2.16}
$$

However, in the case the gyroscope is critically damped or overdamped, the gyroscope should be operated below its resonance frequency ω_0. A suitable frequency of operation is when the damping term of (2.9) becomes equal to the stiffness-related term for small angular rates Ω, and the actuation frequency is chosen half this frequency

$$
2\zeta\omega_0\omega = \omega_0^2, \quad \text{giving} \quad \omega = \frac{\omega_0}{2\zeta}. \tag{2.17}
$$

By operating the device in such a way, in both the drive and sense mode the factor 2ζ drops, but the expression for the Coriolis torque given by (2.13) remains unchanged. Therefore, by this analysis, the ratio of the drive and sense mode amplitudes of a gyroscope is equal for all classes of damping.

The performance of a gyroscope is also to be determined by its response time; besides a sensitive sensory system, also the ability to quickly respond to changes in angular rate Ω classifies the system. The corresponding response time τ_{95}—a measure for agility—is calculated from the second-order differential equation, describing the mechanical behaviour of the system in response to a torque step function. Here, we assume that the gyroscope is driven in steady state with frequency ω, the coupling from sense to drive mode is negligible, and an angular rate Ω is applied stepwise ($v = 0$). In that case, the governing equation for analysing transients in the sense mode becomes

$$
\frac{\mathrm{d}^2\varphi(t)}{\mathrm{d}t^2} + 2\zeta\omega_0\frac{\mathrm{d}\varphi(t)}{\mathrm{d}t} + (\omega_0^2 - \Omega_0^2)\varphi(t) = 2\omega\Omega_0\vartheta_0\sin(\omega t)H(t), \tag{2.18}
$$

where $H(t)$ denotes the Heaviside step function. The general solution of this damped second-order system is

$$
\varphi(t) = \Phi_1 e^{-r_1 t} + \Phi_2 e^{-r_2 t}, \tag{2.19}
$$

where Φ_1 and Φ_2 need to be derived from initial conditions and r_1 and r_2 are given by

$$
r_{1,2} = \zeta\omega_0 \pm \sqrt{\zeta^2\omega_0^2 - \omega_0^2 + \Omega_0^2}, \tag{2.20}
$$

which simplifies under the condition $\Omega_0 \ll \omega_0$ to

$$
r_{1,2} \approx \omega_0\left(\zeta \pm \sqrt{\zeta^2 - 1}\right). \tag{2.21}
$$

The general solution (2.19) is either real or complex. When the damping ratio ζ is equal or greater than one, the solution is real and the haltere moves without oscillations towards the point of torque equilibrium, dominated by the mathematical term that is responsible for slow changes (minus sign in (2.21)). When the damping ratio ζ becomes smaller than one, the square root term becomes imaginary and the haltere shows overshoot towards its equilibrium, leading to a longer
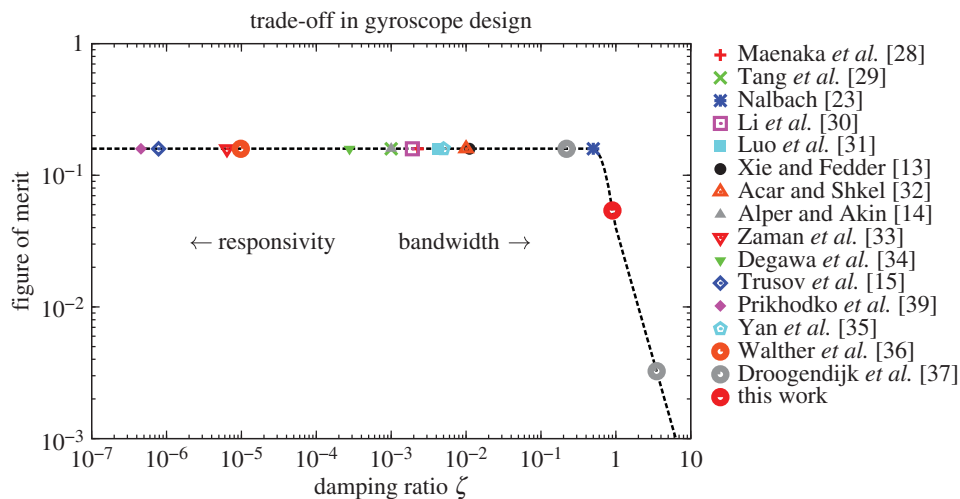
Figure 3. Figure of merit for designing a gyroscopic system. The dashed line indicates the figure of merit by equation (2.27). (Online version in colour.)

stabilization time. The response time τ_{95}, which indicates the time required for the system to reach 95% of its stable final value, is approximated[5] as

$$\tau_{95} \approx \begin{cases} \frac{3}{\zeta\omega_0} & \text{if } \zeta < 0.5, \\ \frac{6\zeta}{\omega_0} & \text{if } \zeta > 1. \end{cases} \quad (2.22)$$

The best response time is obtained when $\zeta = 0.707$, corresponding to a close to critically damped system [26]. However, we observe that nearly all described gyroscopic systems shown in figure 3 are clearly underdamped.

Another consequence of the damping ratio is the impact on the measurement bandwidth $\Delta\omega$ for a gyroscope. From (2.6), we observe that on applying an angular rate Ω with frequency ν, a response is induced in the sense mode at frequencies $\omega \pm \nu$, which can be calculated analytically by using, for example, the method of harmonic balancing as described in [27]. To measure the response, the gyroscope needs sufficient bandwidth $\Delta\omega$

$$\Delta\omega \geq \nu. \quad (2.23)$$

Based on the definition of the quality factor Q, the bandwidth $\Delta\omega$ for underdamped systems is found from the full width at half maximum

$$Q = \frac{\omega_0}{2\Delta\omega}, \quad \text{giving} \quad \Delta\omega = \frac{1}{\kappa}, \quad (2.24)$$

for which $\Delta\omega$ depends inversely on the design parameter κ, and we still assume that the angular rate Ω is small compared with the sensor's resonance frequency ($\Omega_0 \ll \omega_0$), and angular accelerations are small ($\nu \ll \omega$). For overdamped systems, we assume that the system is driven below resonance, and the bandwidth is equal to the frequency of operation, defined in (2.17). Consequently, the bandwidth $\Delta\omega$ becomes

$$\Delta\omega \approx \begin{cases} \zeta\omega_0 & \text{if } \zeta < 0.5, \\ \frac{\omega_0}{4\zeta} & \text{if } \zeta > 1. \end{cases} \quad (2.25)$$

Similar to the response time τ_{95}, a spline interpolation technique can be used to obtain $\Delta\omega$ for all values of ζ.

The sense/drive ratio, the response time and measurement bandwidth are all taken as a criterion for designing a gyroscope. However, these quantities exhibit a similar proportionality with respect to the design parameter κ for

underdamped gyroscopes

$$\tau_{95} \propto \kappa, \quad \mathcal{R} \propto \kappa, \quad \Delta\omega \propto \frac{1}{\kappa}. \quad (2.26)$$

As a consequence, a trade-off exists between the sensitivity parameter $\mathcal{R}$ and the response time τ_{95} and bandwidth $\Delta\omega$ (see also [38]). Namely to have a good sensitivity $\mathcal{R}$, a large κ-value is required, but to obtain a fast and wide-band responding system, κ should be small. For design and analysis, we capture this trade-off in a single number by defining a figure of merit, which is the product of sensitivity and bandwidth

$$\text{figure of merit} = \text{sense/drive ratio} \times \text{bandwidth}$$
$$= \mathcal{R} \times \Delta\omega. \quad (2.27)$$

An overview of several MEMS gyroscopic systems and the blowfly's haltere system [23] is shown in figure 3 by evaluating the figure of merit as a function of the damping ratio ζ. We observe that most MEMS gyroscopes are clearly designed with focus on achieving high responsivity at the cost of bandwidth. Especially, the gyroscopes described in [15,39] show very low damping factors while having a resonance frequency at 2 kHz, being highly sensitive to angular rate, because the ultimate purpose of these two gyroscopes is angle measurement rather than angular rate measurement. Contrarily, the fly's haltere is clearly geared towards a large measurement bandwidth and a fast response. In addition, MEMS-based gyroscopes typically have operating frequencies which are 1 kHz or more, which is significantly higher than the 150 Hz of the blowfly [23]. Note that the figure of merit exhibits a clear decrease when having an overdamped system ($\zeta > 1$), implying that vibratory gyroscopes should preferably be underdamped ($\zeta > 1$).

2.3. Thermal noise

An important characteristic of a sensory system is its signal-to-noise ratio (SNR). Generally, when the SNR is equal or higher than one, a system may enable the detection of the input signal. Hence, besides the responsivity of the sensor, the noise level of the system determines the fundamental detection threshold of the system. To find the detection threshold of our system, we assume a power spectral density
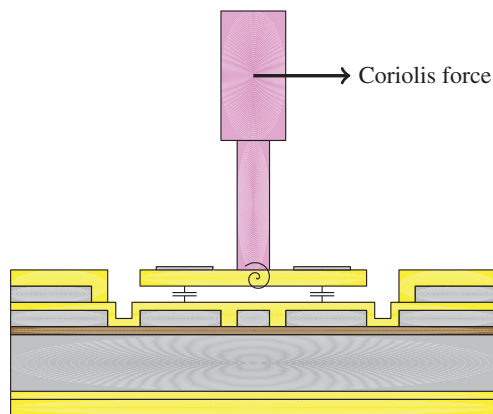
Figure 4. Schematic view of the biomimetic gyroscope (side view). (Online version in colour.)

given by Johnson–Nyquist (thermal) white noise [40]:

$$\bar{T}_n^2 = 4k_B T_0 R, \qquad (2.28)$$

where k_B is the Boltzmann's constant, T_0 is the ambient temperature and $\bar{T}_n^2$ is the square of the noise-induced equivalent torque per unit of bandwidth. The mechanical transfer function $G(\omega)$ of the system determines the resulting mechanical response to the noise

$$G(\omega) = \frac{1}{S - J\omega^2 + jR\omega}. \qquad (2.29)$$

The equivalent noise angle Φ_n is found by integrating the noise power over the full spectrum and taking the square root

$$\Phi_n = \sqrt{\int_0^\infty \bar{T}_n^2 |H(\omega)|^2 d\omega}. \qquad (2.30)$$

The detection threshold Ω_{th} is found by dividing the sensor's equivalent noise angle Φ_n by the rotational angle Φ_m for an angular rate of $1^\circ \, s^{-1}$

$$\Omega_{th} = \frac{\Phi_n}{\Phi_m|_{\Omega_0 = 1^\circ s^{-1}}}. \qquad (2.31)$$

Thermal noise calculations for our haltere-based mechanical system indicate a detection threshold for angular rate sensing of about $0.038^\circ \, s^{-1}$ for frequencies within a bandwidth of 1 kHz.

2.4. Design

The design of the biomimetic gyroscope is based upon the fabrication process for biomimetic hair flow sensors described by Bruinink *et al.* [41] and Dagamseh *et al.* [42] to realize a haltere-based function. Our gyroscope will be actuated in the drive mode with angle ϑ (figure 2) by exploiting electrostatic actuation. Electrostatic forces induced by judiciously chosen AC voltages bring the artificial haltere-like structure in a steady-state resonant rotational motion. Measurement of the Coriolis-induced movement of the artificial haltere-like structure in the sense direction with rotational angle φ is achieved by measuring the differential change in capacitance upon tilt of the artificial haltere (figure 4).

Although we reported on the design and fabrication of such a gyroscope earlier [37], we implemented some important design adjustments here. The suspension of the haltere-based gyroscope is changed to a gimbal-suspension, such as the gyroscope described by Acar & Shkel [32]. In doing so, the effects of
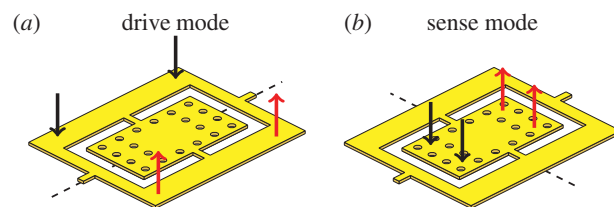
Figure 5. Characteristic modes of the gimbal gyroscope. (Online version in colour.)

residual stress by having a bilayer suspension (i.e. SiRN and Al) can be significantly reduced. In addition, the drive and sense modes become mechanically distinguishable, allowing for a separate optimization of both modes. A schematic view of the two modes for our gimbal suspension is given in figure 5. A disadvantage of such a gimbal design is the difficulty to achieve mode-matching (between drive and sense), which is often aimed for in MEMS gyroscopes to achieve better performance [43,44]. However, for the biomimetic approach followed in this work, the quality factor Q of a gyroscope is relatively low, and consequently mode-matching plays a less pivotal role for the gyroscope's performance.

3. Fabrication

An overview of the design and the fabrication process for the biomimetic gyroscope is shown in figure 6a. The sensor is fabricated on a silicon-on-insulator wafer. Trenches are etched in the silicon device layer using deep reactive-ion etching. A layer of 200 nm stoichiometric Si_3N_4 is used for covering and protecting the trenches. The device layer contains two electrodes, which are used for capacitive read-out of the acceleration-induced movement. On top of the Si_3N_4 layer, a sacrificial layer of poly-silicon (1.5 µm) is deposited by low-pressure chemical vapour deposition. The sensor membrane and springs are constructed by depositing and patterning a 1 µm SiRN layer on top of the poly-silicon. Aluminium (80 nm) is sputtered on top of the membrane to create the electrodes for capacitive read-out. Our haltere-like structure is created by two layers of SU-8, to realize both the centre of mass towards the top of the haltere-like structure and a total haltere length of about 800 µm and an average diameter of about 80 µm. Finally, to release the membrane, the sacrificial poly-silicon layer is removed using XeF_2 etching. The fabrication results are shown by the SEM image in figure 6b.

4. Experimental

4.1. Set-up

To characterize the mechanical properties of the gyroscope, an experimental set-up based on laser Doppler vibrometry [45] is used (figure 7). To measure the rotational modes, we differentially applied a sinusoidal signal superposed to a DC-offset voltage (Delta Elektronika—Power Supply E 030-1) to a pair of electrodes.

4.2. Frequency response

The response for the drive mode (figure 5a) was measured by applying a chirp–voltage in push–pull configuration. The
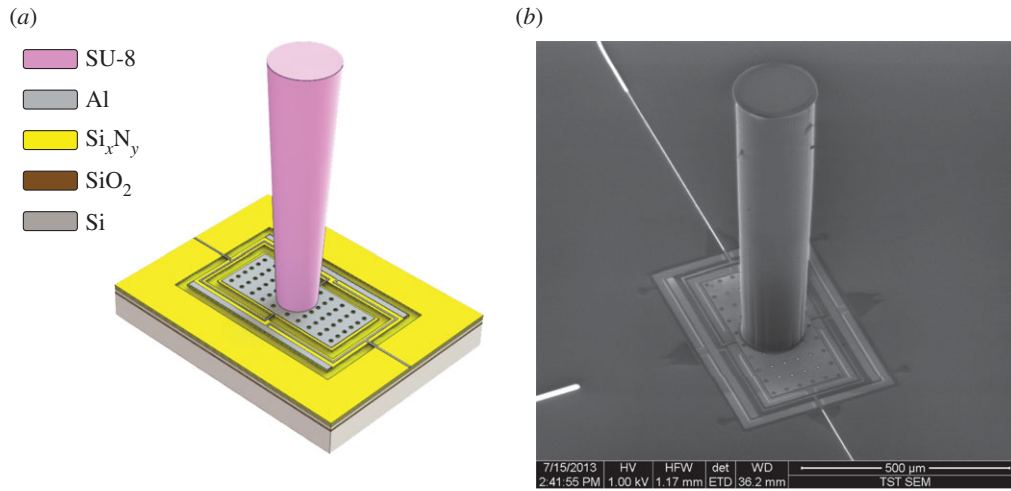
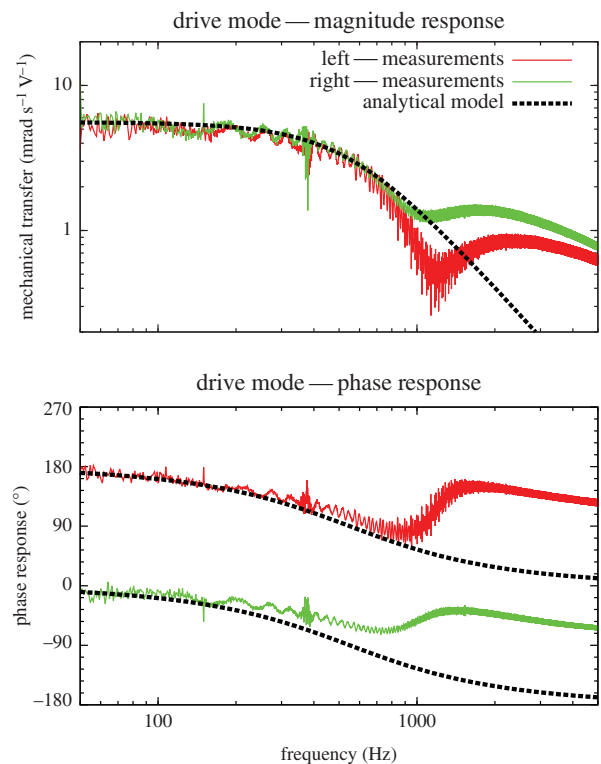**Figure 6.** Design (*a*) and fabrication (*b*) of the MEMS haltere-based gyroscope fabricated by surface micromachining and using SU-8 lithography. (Online version in colour.)
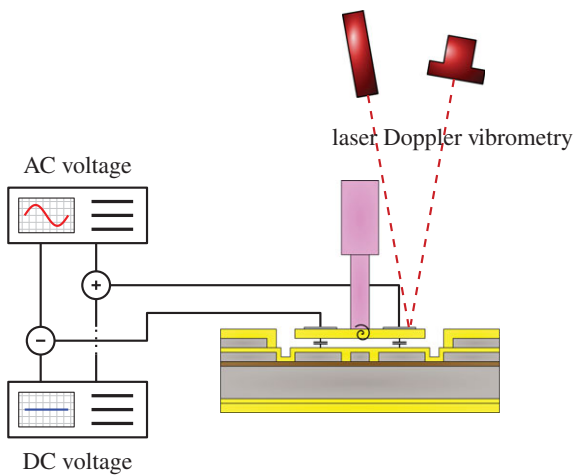
Figure 7. Experimental set-up for characterization of the biomimetic gyroscope. (Online version in colour.)

Figure 8. Optically measured response of the membrane displacement by electrostatically actuating the drive mode ($f_0 = 550$ Hz and $\zeta = 0.9$). (Online version in colour.)

magnitude and phase response are shown in figure 8, both together with the results of an analytical model based on a classical second-order mechanical system. From both figures, the drive mode turns out to be slightly overdamped ($\zeta = 0.9$) with its resonance frequency found at approximately 550 Hz. Owing to the overdamped nature of the system, the bandwidth of the drive mode is calculated by computing the intersection of the stiffness and damping contributing terms in (2.6) and is found to be 305 Hz. Further, we observe that there is a good agreement between the analytical model and the measured response for frequencies up to about 800 Hz.

Similar measurements have been made for the sense mode (figure 5*b*). From figure 9, the sense mode turns out to be slightly overdamped ($\zeta = 1.1$) with its resonance frequency found at approximately 300 Hz. Note that the peaks around this frequency are not owing to mechanical resonance, but are caused by limitations within the used laser Doppler vibrometry set-up. Owing to the over damping, the bandwidth of the sense mode is calculated by computing the intersection of the stiffness and damping contributing terms in (2.6) and is found to be 137 Hz. Further, we observe that there is a good agreement between the analytical model and the measured response for frequencies up to about 2 kHz.

5. Discussion

5.1. Fabrication

Regarding the fabrication process, the SEM image from the biomimetic gyroscope (figure 6*b*) shows that we have successfully fabricated artificial haltere-like structures with increased mass at the top. Optical measurements indicate that the haltere length is about 800 μm, and that the haltere-like structures have a slight negative tapering towards the membrane. This tapering results from the light intensity profile during exposure of the SU-8 as well as the two-step lithography process incorporated in the design. This
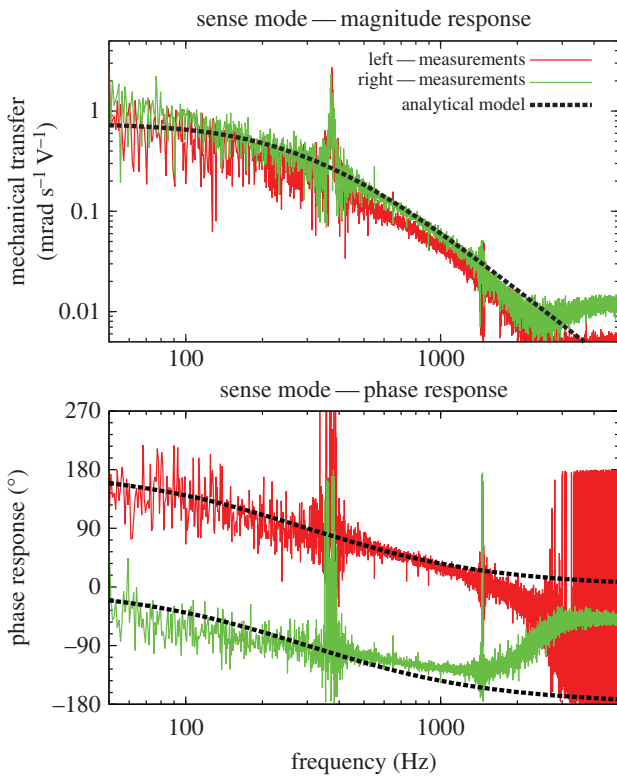
Figure 9. Optically measured response of the membrane displacement by electrostatically actuating the sense mode ($f_0 = 300$ Hz and $\zeta = 1.1$). (Online version in colour.)

effectively causes the centre of mass to be located in the upper part of the haltere-like structures, similar to the fly's haltere (figure 1).

5.2. Modal response

The measured resonance frequency for the drive mode was measured to be about 510 Hz with a damping ratio of $\zeta = 0.9$. Although this resonance frequency is slightly higher than the wing-beat frequency of the fly (130–150 Hz), it remains in the same order of magnitude. Similar results are obtained for the sense mode, wherein the resonance frequency was found to be about 300 Hz with a slightly overdamped system ($\zeta = 1.1$).

However, we observed that for both the measured drive and sense mode the response is a combination of modes, especially for higher excitation frequencies. Because every mode is expected to be about critically damped, it is difficult to identify each modal resonance frequency owing to the absence of clear resonance peaks and phase shifts. Theoretically, using capacitive differential read-out techniques, the contributions of the drive and vertical mode can be commonly rejected for measurement of the sense mode.

5.3. Biomimetic approach

A haltere-inspired gyroscope has been designed, fabricated and partially characterized. However, we were not able to experimentally demonstrate its response to externally applied angular rates using our in-house-built rate-table, electrostatic actuation of the drive mode, and capacitive read-out of the sense mode. With the current design and

the maximum applicable angular rate using our rate table (rate amplitude of about $3000° \, s^{-1}$ at a frequency of 14 Hz), the calculated displacement of the membrane edges for capacitive read-out of the sense mode is in the order of nm, which corresponds to the measurement threshold of our read-out electronics [46].

The high damping ratio ζ for this type of gyroscope results in two difficulties for rate measurements. First, following (2.26) from our design analysis a trade-off exists between responsivity (ratio drive/sense mode), and bandwidth and response time. Clearly, a high damping ratio has a negative impact on the responsivity, thus requiring a relatively large drive angle amplitude for a given sense angle amplitude. In addition, when having a critically or overdamped electrostatically driven system, the driving can be considered quasi-statically (i.e. operating well below resonance). For a torsional electrostatic actuator, the maximum achievable drive angle ϑ, while preventing pull-in[6] is [47]

$$\vartheta = 0.4404 \, \vartheta_0, \quad \text{with} \quad \vartheta_0 = \arctan\left(\frac{g_m}{L_{drive}}\right), \quad (5.1)$$

where g_m is the gap between the gimbal and the substrate, L_{drive} is half the length of the gimbal in the drive direction and ϑ_0 is the maximum mechanical angle at which the gimbal hits the lower substrate. To compare, when the system is underdamped and electrostatically driven at resonance, the gimbal's rotation is amplified by the system's quality factor (i.e. a dimensionless parameter that describes how underdamped the system is), resulting in a larger amplitude for the sense mode, but smaller bandwidth and increased response time.

Generally, we believe that a working biomimetic gyroscope following the 'design rules' of a fly and the use of MEMS technology is difficult to achieve, but possible. However, this will require adaptation of the design and the fabrication process. For our gyroscope, in particular, the value of $\mathcal{R}$ needs to be increased in order to measure the applied angular rates. A possibility is the use of piezo-resistive sensing instead of capacitive read-out, as proposed by Wicaksono et al. [21]. In addition, improvement of the mechanical gimbal-suspension and the use of more compliant materials will help to increase $\mathcal{R}$. One could also think of exchanging the technology of MEMS for another type of technology (e.g. three-dimensional printing) and investigate its potential for biomimetic gyroscopes.

5.4. Comparison with the fly's haltere

To compare the biomimetic gyroscope with the fly's haltere, several performance metrics of the fly's haltere are identified. First, the moment of inertia J is calculated based on the values given by Nalbach [23], wherein the mass is considered as a point mass at distance r_h from the axis of rotation. Considering the fly's haltere to be slightly underdamped ($\zeta = 0.5$), the resonance frequency f_0, torsional stiffness and torsional damping can be calculated based on a natural frequency of 150 Hz [9]. From these parameters, performance metrics as response time and sense/drive ratio are calculated. An overview of all parameters and performance metrics with their values is shown in table 1. Also the values for the haltere-inspired gyroscope are listed, wherein most values are theoretical.

From table 1, nearly all values for the haltere-inspired MEMS gyroscope are on the same order as those of the fly's halteres. We observe that the haltere-based gyroscope is geared towards large bandwidth and short response time

Table 1. Characteristics of the fly's haltere based on [23] and the biomimetic gyroscope. Values marked with an asterisk are measured quantities, others are calculated from geometry, materials properties, or are derived from dynamic characterization.

quantity	symbol	fly	this work (drive)
haltere			
length	r_h	1.07 mm	0.8 mm
mass	m_h	5.89×10^{-9} kg	2.29×10^{-8} kg
characteristics			
damping ratio	ζ	0.5	0.9*
resonance frequency	f_0	210 Hz	550 Hz*
parameters			
torsional stiffness	S	1.17×10^{-8} Nm rad^{-1}	4.89×10^{-8} Nm rad^{-1}
torsional damping	R	8.90×10^{-12} Nm s rad^{-1}	2.79×10^{-11} Nm s rad^{-1}
moment of inertia	J	6.74×10^{-15} kg m^2	4.93×10^{-15} kg m^2
performance			
response time	τ_{95}	4.55 ms	~1.2 ms
sense/drive ratio	$\mathcal{R}$	2.65×10^{-5} degree^{-1} s^{-1}	5.61×10^{-6} degree^{-1} s^{-1}
bandwidth (sense)	$\Delta\omega$	105 Hz	137 Hz
detection threshold	Ω_{th}	$0.038°$ s^{-1}	$0.018°$ s^{-1}
drive angle	ϑ_{max}	$85°$	$0.5°$

rather than achieving a high sense/drive ratio $\mathcal{R}$, which is also exhibited by the figure of merit (figure 3). Note that to achieve sufficient rotation in the sense mode the fly's halteres operate under large drive angles with amplitudes up to $85°$, whereas the maximum achievable drive amplitude for the MEMS gyroscope is only $0.5°$. As a consequence, the response in sense direction, which is linearly related to the drive amplitude, is significantly larger for the fly's haltere than for our MEMS counterpart. Furthermore, by having these large drive amplitudes, the fly is also able to measure angular rates for all three planes: roll, pitch and yaw [23].

The response time for the fly is theoretically calculated to be about 4.5 ms, which is in the order of the fly's latency (less than 5 ms) for making compensatory head movements [48]. Because this behavioural response latency includes the time, it takes the neck motor system to exert sufficient muscle power to move the head, the pure sensor delay at the level of the campaniform sensilla would clearly be shorter than 5 ms [49,50]. Although thermal noise plays an important role in the flow-sensitive filiform hairs of crickets [51], we do not believe that thermal noise matters for angular rate measurement. Hengstenberg [52] showed that below angular rates of $50°$ s^{-1} no body motion of the fly was observed in absence of visual clues. In addition, Hengstenberg showed that the fly is able to respond to angular step stimuli of up to $2000°$ s^{-1}, indicating that the fly tends to respond to large variations in angular rate Ω rather than to small angular rates. Additionally, the low sensitivity of the halteres for small angular rates is compensated for by the visual system processing optic flow [53].

6. Conclusion

Inspired by the fly's haltere, a biomimetic gimbal-based gyroscope has been designed, fabricated and partially

characterized. Design rules for gyroscopes were investigated and it was shown that the fly's halteres tend to emphasize a large measurement bandwidth and a fast response, rather than a high responsivity or low detection threshold, by having a relatively low-quality factor. Measurements on our haltere-inspired sensors indicate an excitable gyroscope with a (drive mode) resonance frequency of about 550 Hz and a damping ratio of 0.9. A response to externally applied angular rates is not demonstrated owing to the limited applied rotation rates and the very small induced sense mode amplitude, which is mainly caused by the structures being overdamped and the small achievable drive-mode amplitudes; our haltere-inspired gyroscope is physically limited to drive angles of about $0.5°$, which is much smaller than the fly's drive angles (up to $85°$). Future research focuses on testing the performance of artificial haltere-inspired sensors as a function of external rotations by, for example, improving the design or exploiting different technology.

Endnotes

[1]In this work, all gyroscopes are so-called Coriolis vibratory gyroscopes, which are in fact angular rate sensors. By integration of the measured angular rate, information about the angle is obtained.
[2]Damping is caused by a force opposing movement, in proportion to an object's velocity, which has the effect of hampering mechanical movement.
[3]This torque is delivered by electrostatic actuation in the case of the MEMS gyroscope and by the muscles of the flight motor in case of the fly.
[4]This ratio is related to the scale factor of MEMS gyroscopes by taking the transfer by capacitive read-out into account [25].
[5]A precise mathematical solution is rather involved. A spline interpolation is used for connecting the two asymptotes smoothly and obtaining a good approximation, which is not shown here.
[6]Pull-in is the effect that a transducer transverses state-space beyond its stable region accompanied by a fast transition to an irreversible constrained state, e.g. when two mechanical parts collide.

References

1. Liu C. 2007 Micromachined biomimetic artificial haircell sensors. *Bioinspir. Biomim.* **2**, 162–169. (doi:10.1088/1748-3182/2/4/S05)

2. Horn E, Bischof H-J. 1983 Gravity reception in crickets: the influence of cereal and antennal afferences on the head position. *J. Comp. Physiol. A* **150**, 93–98. (doi:10.1007/BF00605292)

3. Tobias M, Murphey RK. 1979 The response of cercal receptors and identified interneurons in the cricket (*Acheta domesticus*) to airstreams. *J. Comp. Physiol. A* **129**, 51–59. (doi:10.1007/BF00679911)

4. Shimozawa T, Kanou M. 1984 Varieties of filiform hairs: range fractionation by sensory afferents and cercal interneurons of a cricket. *J. Comp. Physiol. A* **155**, 485–493. (doi:10.1007/BF00611913)

5. Fraenkel G, Pringle JWS. 1938 Biological sciences: halteres of flies as gyroscopic organs of equilibrium. *Nature* **141**, 919–920. (doi:10.1038/141919a0)

6. Pringle JWS. 1948 The gyroscopic mechanism of the halteres of Diptera. *Phil. Trans. R. Soc. Lond. B* **2330**, 347–384. (doi:10.1098/rstb.1948.0007)

7. Hengstenberg R. 1998 Controlling the fly's gyroscopes. *Nature* **392**, 757–758. (doi:10.1038/33796)

8. Sandeman DC, Markl H. 1980 Head movements in flies (*Calliphora*) produced by deflexion of the halteres. *J. Exp. Biol.* **85**, 43–60.

9. Nalbach G, Hengstenberg R. 1994 The halteres of the blowfly *Calliphora*—II. Three-dimensional organization of compensatory reactions to real and simulated rotations. *J. Comp. Physiol. A* **175**, 695–708. (doi:10.1007/BF00191842)

10. Chan WP, Prete F, Dickinson MH. 1998 Visual input to the efferent control system of a fly's 'gyroscope'. *Science* **280**, 289–292. (doi:10.1126/science.280.5361.289)

11. Ristroph L, Bergou AJ, Ristroph G, Coumes K, Berman GJ, Guckenheimer J, Wang ZJ, Cohen I. 2010 Discovering the flight autostabilizer of fruit flies by inducing aerial stumbles. *Proc. Natl Acad. Sci. USA* **1070**, 4820–4824. (doi:10.1073/pnas.1000615107)

12. Yazdi N, Ayazi F, Najafi K. 1998 Micromachined inertial sensors. *Proc. IEEE* **860**, 1640–1659. (doi:10.1109/5.704269)

13. Xie H, Fedder GK. 2003 Fabrication, characterization, and analysis of a DRIE CMOS–MEMS gyroscope. *IEEE Sens. J.* **30**, 622–631.

14. Alper SE, Akin T. 2005 A single-crystal silicon symmetrical and decoupled MEMS gyroscope on an insulating substrate. *J. Microelectromech. Syst.* **140**, 707–717. (doi:10.1109/JMEMS.2005.845400)

15. Trusov AA, Prikhodko IP, Zotov SA, Shkel AM. 2011 Low-dissipation silicon tuning fork gyroscopes for rate and whole angle measurements. *IEEE Sens. J.* **110**, 2763–2770. (doi:10.1109/JSEN.2011.2160338)

16. Rosner R, Egelhaaf M, Grewe J, Warzecha AK. 2009 Variability of blowfly head optomotor responses. *J. Exp. Biol.* **212**, 1170–1184. (doi:10.1242/jeb.027060)

17. Wu W-C, Wood RJ, Fearing RS. 2002 Halteres for the micromechanical flying insect. In *Proc. ICRA 2002*, pp. 60–65. Washington, DC, USA. Piscataway, NJ: IEEE.

18. Wu W-C, Wood R. 2006 Angular rate sensor using electromechanical haltere. Patent no. US 7107842.

19. Tang TK *et al*. 1997 A packaged silicon MEMS vibratory gyroscope for microspacecraft. In *Proc. MEMS 1997*, pp. 500–505. Nagoya, Japan. Piscataway, NJ: IEEE.

20. Challoner AD, Gutierrez RC, Tang TK. 2007 Cloverleaf microgyroscope with electrostatic alignment and tuning. Patent no. US 7159441.

21. Wicaksono DHB, Chen Y, French PJ. 2007 Design and modelling of a bio-inspired MEMS gyroscope. In *Proc. ICEEI*, pp. A–05. Bandung, Indonesia: Institut Teknologi Bandung.

22. Smith GL, Bedair SS, Schuster BE, Nothwang WD, Pulskamp JS, Meyer CD, Polcawich RG. 2012 Biologically-inspired, haltere, angular-rate sensors for micro-autonomous systems. In *Proc. SPIE*, vol. 8373, pp. 83731K. Bellingham, WA: SPIE.

23. Nalbach G. 1993 The halteres of the blowfly *Calliphora*—I. Kinematics and dynamics. *J. Comp. Physiol. A* **173**, 293–300. (doi:10.1007/BF00212693)

24. Zotov SA, Trusov AA, Shkel AM. 2011 Demonstration of a wide dynamic range angular rate sensor based on frequency modulation. In *Proc. IEEE Sensors 2011*, pp. 149–152. Limerick, Ireland. Piscataway, NJ: IEEE.

25. IEEE Aerosp. 2001 Electron. Sys. Soc. IEEE standard for inertial sensor terminology. *IEEE Std*. 528–2001.

26. Shinners SM. 1998 *Modern control system theory and design*, 2nd edn. London, UK: John Wiley & Sons, Inc.

27. Cartmell M. 1990 *Introduction to linear, parametric and nonlinear vibrations*, 1st edn. London, UK: Chapman and Hall.

28. Maenaka K, Fujita T, Konishi Y, Maeda M. 1996 Analysis of a highly sensitive silicon gyroscope with cantilever beam as vibrating mass. *Sens. Actuators A, Phys.* **54**, 568–573. (doi:10.1016/S0924-4247(97)80016-7)

29. Tang TK, Gutierrez RC, Wilcox JZ, Stell C, Vorperian V, Calvet R, Li WJ, Chakraborty I, Bartman R. 1996 Silicon micromachined vibratory gyroscope. In *Proc. Solid-State Sensor and Actuator Workshop*, pp. 288–293. Hilton Head Island, SC, USA. Piscataway, NJ: IEEE.

30. Li X, Bao M, Yang H, Shen S, Lu D. 1999 A micromachined piezoresistive angular rate sensor with a composite beam structure. *Sens. Actuators A, Phys.* **72**, 217–223. (doi:10.1016/S0924-4247(98)00220-9)

31. Luo H, Fedder GK, Carley LR. 2000 An elastically gimbled *z*-axis CMOS–MEMS gyroscope. In *Proc. IS3M*, pp. 1–6. Hong Kong.

32. Acar C, Shkel AM. 2004 Structural design and experimental characterization of torsional micromachined gyroscopes with non-resonant drive mode. *J. Micromech. Microeng.* **14**, 15–25. (doi:10.1088/0960-1317/14/1/303)

33. Zaman MF, Sharma A, Hao Z, Ayazi F. 2008 A mode-matched silicon-yaw tuning-fork gyroscope with subdegree-per-hour Allan deviation bias instability. *J. Microelectromech. Syst.* **170**, 1526–1536. (doi:10.1109/JMEMS.2008.2004794)

34. Degawa M, Jeong HW, Sonobe H, Takubo C, Yamanaka K, Goto Y. 2009 Laterally-driven deformation-robust MEMS gyroscopes with three sets of symmetrically arranged folded-beam suspensions. In *Proc. Transducers '09*, pp. 664–667. Denver, CO, USA. Piscataway, NJ: IEEE.

35. Yan L, Shangchun F, Zhanshe G, Jing L, Le C. 2012 Study of dynamic characteristics of resonators for MEMS resonant vibratory gyroscopes. *Microsyst. Technol.* **18**, 639–647. (doi:10.1007/s00542-012-1492-2)

36. Walther A, Desloges B, Lejuste C, Coster B, Audebert P, Willemin J. 2013 Development of a 3D capacitive gyroscope with reduced parasitic capacitance. *J. Micromech. Microeng.* **23**, 025013. (doi:10.1088/0960-1317/23/2/025013)

37. Droogendijk H, Brookhuis RA, de Boer MJ, Sanders RGP, Krijnen GJM. 2012 Design and fabrication of a biomimetic gyroscope inspired by the fly's haltere. In *Proc. IEEE Sensors 2012*, pp. 1400–1403. Taipei, Taiwan. Piscataway, NJ: IEEE.

38. Apostolyuk VA, Logeeswaran VJ, Tay FEH. 2002 Efficient design of micromechanical gyroscopes. *J. Micromech. Microeng.* **12**, 948–954. (doi:10.1088/0960-1317/12/6/327)

39. Prikhodko IP, Zotov SA, Trusov AA, Shkel AM. 2011 Sub-degree-per-hour silicon MEMS rate sensor with 1 million Q-factor. In *Proc. Transducers '11*, pp. 2809–2812. Beijing, China. Piscataway, NJ: IEEE.

40. Gabrielson TB. 1993 Mechanical thermal noise in micromachined acoustic and vibration sensors. *IEEE Trans. Electron. Devices* **40**, 903–909. (doi:10.1109/16.210197)

41. Bruinink CM, Jaganatharaja RK, de Boer MJ, Berenschot JW, Kolster ML, Lammerink TSJ, Wiegerink RJ, Krijnen GJM. 2009 Advancements in technology and design of biomimetic flow-sensor arrays. In *Proc. MEMS 2009*, pp. 152–155. Piscataway, NJ: IEEE.

42. Dagamseh A, Lammerink T, Sanders R, Wiegerink R, Krijnen G. 2011 Towards high-resolution flow cameras made of artificial hair flow-sensors for flow pattern recognition. In *Proc. MEMS 2011*, pp. 648–651. Cancun, Mexico. Piscataway, NJ: IEEE.

43. Hu ZX, Gallacher BJ, Burdess JS, Fell CP, Townsend K. 2011 Precision mode matching of MEMS gyroscopes by feedback control. In *Proc. IEEE Sensors 2011*, pp. 16–19. Limerick, Ireland.

44. Sonmezoglu S, Alper SE, Akin T. 2012 An automatically mode-matched MEMS gyroscope with 50 Hz bandwidth. In *Proc. MEMS 2012*, pp. 523–526. Paris, France. Piscataway, NJ: IEEE.

45. Polytec. 2005 *MSA-400 micro system analyzer*. Waldbronn, Germany: Polytec.

46. Dagamseh AMK, Bruinink CM, Wiegerink RJ, Lammerink TSJ, Droogendijk H, Krijnen GJM. 2013 Interfacing of differential-capacitive biomimetic hair flow-sensors for optimal sensitivity. *J. Micromech. Microeng.* **23**, 035010. (doi:10.1088/0960-1317/23/3/035010)

47. Nielson GN, Barbastathis G. 2006 Dynamic pull-in of parallel-plate and torsional electrostatic MEMS actuators. *J. Microelectromech. Syst.* **150**, 811–821. (doi:10.1109/JMEMS.2006.879121)

48. Hengstenberg R, Sandeman DC, Hengstenberg B. 1986 Compensatory head roll in the blowfly *Calliphora* during flight. *Proc. R. Soc. Lond. B* **2270**, 455–482. (doi:10.1098/rspb.1986.0034)

49. Dickinson MH. 1990 Comparison of encoding properties of *Campaniform sensilla* on the fly wing. *J. Exp. Biol.* **151**, 245–261.

50. Fox JL, Daniel TL. 2008 A neural basis for gyroscopic force measurement in the halteres of *Holorusia*. *J. Comp. Physiol. A* **194**, 887–897. (doi:10.1007/s00359-008-0361-z)

51. Shimozawa T, Murakami J, Kumagai T. 2003 Cricket wind receptors: thermal noise for the highest sensitivity known. In *Sensors and sensing in biology and engineering* (eds FG Barth, JAC Humphrey, TW Secomb), pp. 145–159. Berlin, Germany: Springer.

52. Hengstenberg R. 1991 Gaze control in the blowfly *Calliphora*: a multisensory, two-stage integration process. *Neurosciences* **3**, 19–29.

53. Taylor GK, Krapp HG. 2007 Sensory systems and flight stability: what do insects measure and why? *Adv. Insect Physiol.* **34**, 231–316. (doi:10.1016/S0065-2806(07)34005-8)